Post-Print

This is the accepted version of:

When citing this work, cite the original published paper.

Aerodynamic Analysis of an Unmanned Cyclogiro Aircraft

Louis Gagnon, Giuseppe Quaranta

Department of Aerospace Science and Technology, Politecnico di Milano, Milano, Italy

Meinhard Schwaiger, David Wills

Innovative Aeronautics Technologies GmbH, Linz, Austria

Abstract

Very little is currently known of the aerodynamic interaction between neighboring cycloidal rotors. Such knowledge is, however, of crucial importance to tune the controller and rotor disposition of a cyclogiro aircraft. Thus, a three-dimensional Computational Fluid Dynamics (CFD) model is developed, validated, and used to analyze the D-Dalus L1 four-rotor unmanned aircraft operating under several configurations. The model solves the Euler equations using the OpenFOAM toolbox in order to provide fast results on a desktop computer. Validation is performed against thrust forces and flow streamlines obtained during wind tunnel experiments at various flight velocities. Numerical results from CFD match the trends of the experimental data. Flow behavior matches the video footage of the wind tunnel tests. Although boundary layer effects are neglected, satisfactory results are obtained both qualitatively and quantitatively. This paper concentrates on the results while a companion paper covers the model development. It is found that rotor flow, efficiency, and interaction with the airframe is considerably different between hover and forward flight conditions. It is also confirmed that the same flow particle hits the rotor blades more than once and thus generates strong inner vortices. High pitch magnitudes lead to excessive power consumption while not significantly improving the thrust. CFD is able to model the effects of dynamic pitching, the vortices inside the rotor, and the 3D flow towards the endplates. Finally, airframe modifications for less flow blockage, higher rear rotors, and an adapted pitching schedule may bring considerable efficiency increases to the studied cyclogiro.

Introduction

Cycloidal rotors are often referred to as cycloidal propellers, cyclogiros, cyclorotors, or cyclogyro and sometimes even as vertical axis propellers. They propelled airships [1, 2, 3, 4], aircraft [5, 6, 7], micro aircraft [8, 9, 10, 11], and boats [12]. They are also used for wind [13, 14, 15, 16] and water [14, 16] turbines and there are claims that they could propel submarines [1].

A cycloidal rotor is the assembly of blades disposed to form a cylinder and rotate about the axis of that cylinder. It is similar to a H-Darrieus wind turbine. An example rotor is shown in Fig. 1. The rotation of the blades is such that their span axes always remain parallel to the axis of the cylinder. The blades also pitch individually about their own pivoting axis and this occurs synchronously with the main rotation. Together, these motions generate a total thrust that can be directed anywhere on a plane perpendicular to the span axes of the blades. The thrust direction can be changed almost instantly by changing the pitch control phase or magnitude. The pitching is

Figure 1: Cycloidal rotor.

usually imposed to the blades by a set of rigid links called the pitch rods and shown in Fig. 2. These pitch rods are offset from the axis of the cylinder and thus impose a cyclic pitching motion to the blades.
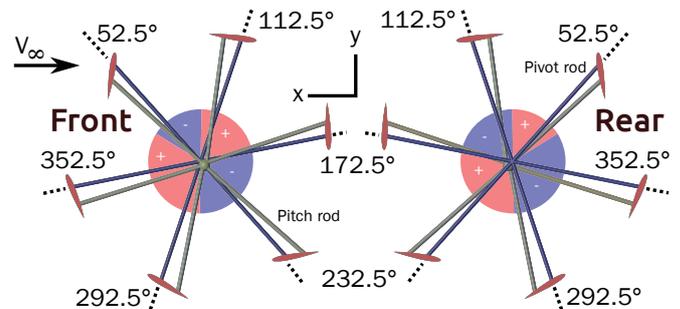
Figure 2: Rotor configuration with motion transmitting links in blue (pivot rod) and pitch control links in green (pitch rod). The underlying disks show the zones where the forward velocity augments, in red (+), and diminishes, in blue (-), the angle of attack of the blade.

The D-Dalus L1 [17] is an unmanned aerial vehicle prototype which is able to hover and which relies only on cycloidal rotors for thrust generation [18, 19, 20]. The D-Dalus L1 is shown in Fig. 3 and a sketch of its rotors as seen from the left was shown in Fig. 2. The cycloidal rotors should allow it to travel at higher forward velocities than helicopters. This unmanned aircraft is the subject of the present study and the dimensions of the airframe and the imposed parameters are given in Table 1.

The research currently available on the 3D aerodynamic modeling of cycloidal propellers is limited. The CFD models developed
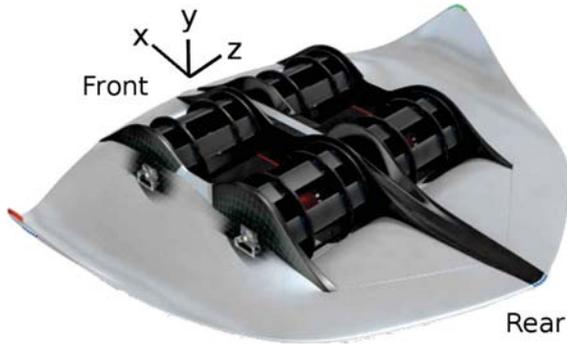
Figure 3: D-Dalus L1 prototype.

Table 1: D-Dalus L1 parameters

blade chord	0.060 m
blade span	0.24 m
rotor diameter (center of spider to pitching axis on blade)	0.24 m
pitch axis distance from nose of blade	0.02577 m
longitudinal distance between centers of front and rear rotors	0.556 m
lateral distance between midspan of rotor and aircraft symmetry plane	0.2505 m
approximative NACA number of the blades	0016
blade local pitch angle range	[-37°, 35°]
phase angle[a]	37.5°
airframe angle of attack	0°
endplates thickness	0.01 m
endplates diameter	0.29 m

[a]The phase angle is the angle between the negative y-axis and the pivot arm at the position of maximum local blade pitch angle; it occurs prior to reaching the bottommost blade position.

by [21, 22, 23, 14, 11, 24, 25, 26, 6] are all two-dimensional. [11] notes that the flow at midpsan and forces of a single rotor subjected to inflow is well represented by a 2D CFD model. They report interaction between blades near the position of peak force. However, [24] mentions that the flow is highly three-dimensional They rely on the k-ω-SST turbulence model with a RANS CFD method. They also used a deforming mesh along with mesh refinement and 400 steps per rotation. [6] report that a 3D model would reduce the uncertainty of the CFD modeling of cycloidal rotors. [24] also mentions that high magnitude pitching functions make a solution without CFD unfeasible. [27] developed both 2D and 3D CFD models and concludes that cycloidal rotor flow is highly three-dimensional and that the 2D code fails to grasp most of the flow unsteadiness. [28] also use a 3D CFD model for a vertical wind turbine without blade pitching. Finally, there is also the virtual camber effect reported by [3], [27] and [29] which is caused by the circular path of the blades and is automatically taken into consideration by CFD. This path implies that even when not pitching about its pivot point, the blade has different angles of attack at different positions along its chord.

It is thus clear that a 3D model is important if the interaction between four rotors and an airframe is to be understood. This article first present the three-dimensional CFD model which was developed. The start from a previous rotor study, the evolution into a full-aircraft model, and the validation is covered in the Model Development section. It ends by presenting the 7 post-validation cases that were studied. A thorough scrutiny of the flow for each case is presented in the Results section. It is based on the instantaneous and mean forces and the flow field visualization. Supplementary video material is made available online and is presented in APPENDIX B. All data shown in this article has been normalized and the same normalization values and field scales are used throughout the paper. The normalization is necessary to preserve the trade secrets of the company. The

Discussion and Conclusion sections provide a perspective on the results obtained by relating them to current literature and to the initial goals. Finally, the outcome of this study allows to refine the current aircraft design by minimizing the harmful rotor interactions and exploiting the beneficial ones based on the results presented here.

Model Development

The CFD model is an improved version of a previous cycloidal rotor model [30]. It comes from a proof of concept 3D CFD simulation of a cycloidal rotor produced within the CROP [31] consortium. Cases both with and without endplates were tested and agreed with the forces from the experimental data made available for one rotor. However, modeling the endplates yielded a better qualitative comparison with experimental observations. That first model was then tuned to increase its stability at a range of angular velocities and refine the mesh resolution around the flow vortices.

The current model is a three-dimensional CFD Euler laminar simulation. Consequently, viscosity is not included in the equations and no wall boundary layer will form. Nevertheless, Euler is chosen in order to maintain a short turnover time and thus allow running more cases during the project. It is considered a good compromise without resorting to RANS or better wall treatment methods. Furthermore, as pointed out by [24], the turbulence models used by most authors are unable to properly represent the strong separation zones on the blades. This study does not model turbulence in any simulation because, to properly model separation, a considerably finer grid would be required near the walls. And consequently, such a finer grid in the critical boundary layer zone would cause considerably longer simulation times because of its impact on the Courant number. Using a Euler laminar simulation allows for 3D simulations while respecting the computer-time constraints of the project and knowing that comparable uncertainties still occur with higher-end models due to the presence of severe separation.

The PIMPLE algorithm from the open source OpenFOAM toolkit is used and it is similar to that used by [24] for cycloidal rotors. The six blades of the rotor are inserted into a double embed oscillating moving mesh interface referred to as the Arbitrary Mesh Interface (AMI). Both the double embedded moving mesh algorithm and an accompanying no-slip boundary condition necessary for cyclogyro simulations were previously created [32] and publicly released [33, 34].

The number of cells used for a rotor alone is roughly 1 million while in the absence of endplates the number decreases to 350 thousand. This is mostly due to the presence of the interfaces of the oscillating mesh which leaves a limited amount of space between the rotor blades, the blade mesh-interfaces, the endplates, and the rotor mesh-interfaces. Effectively, a sliding interface is located in the space between the endplates and the individually oscillating blades, which is only 3% of the blade span. Furthermore, an equally small gap hosts the rotor sliding interface which is located between the endplates and the airframe.

The single rotor model matched the forces and flow geometry obtained experimentally. It was then combined with a second rotor in order to reproduce two of the aircraft rotors. Then, a symmetry plane was used on the x-y midplane to model the whole aircraft without increasing the total number of cells required. The simulations are run using a first harmonic sinusoidal pitching schedule function equivalent to the physical pitching schedule of the aircraft. That pitching function is sinusoidal and its frequency matches the angular velocity of the rotor. To match the reality of the physical aircraft, an offset is applied to the pitch function to increase the pitch angle magnitude on the bottom part of the rotation cycle. Finally, a phase angle is also used to anticipate the position of maximum pitch with respect to the bottommost angular position.

Several design iterations were undertaken because the mesh zones between the various AMI, the endplates, and the airframe were all very sensitive to the meshing parameters. The most extreme case expected to be encountered during the simulations had an airframe angle of attack (AoA) of 15°, a horizontal incoming wind velocity of 30 m/s, and a mesh size of 2.7M cells prior to refinements. A simulation with these parameters was used to verify the ability to run the simulation consistently. Once a stable analysis method was thus obtained, the geometry and simulation parameters were validated against the wind tunnel data. The thorough description of the model, boundary conditions, numerical methods, and mesh generation process are given in a different publication [35].

Experimental Data

An unpublished experimental campaign where the D-Dalus L1 aircraft was run inside a wind tunnel provided the data against which the final CFD model was calibrated. The campaign took place at Technische Universität München in Germany. The collected data consists of longitudinal (F_x) and vertical (F_y) forces on the whole aircraft. They were measured for incoming winds that simulated forward velocities of 10 m/s, 15 m/s, 20 m/s, and 25 m/s. The rotor velocities were set to 3970 RPM and air density was 1.2 kg/m^3. A hover pitching schedule was used during the wind tunnel tests. Due to an unpredictable circumstance, the rear rotors of the aircraft were not powered. The development of a CFD method for free rotation of the double embed rotating AMI was not possible within the project's time frame. Thus, the CFD model was validated using an approximated rear rotor velocity. Nevertheless, this approximation comes from a series of tests made at various rotor velocities, as described below.

Validation

Validity of the model was a fundamental concern throughout the study. Thus, an attentive iterative design procedure was presented so far. It evolved from a previously validated rotor model [30] by carefully designing the airframe mesh [35]. The resulting model is validated qualitatively, as reported in the companion paper [35]. To further ensure validity of the model, this section presents both an investigation on the rear rotor velocity and a verification that the trends of the generated forces follow the experimental data as the forward flight velocity increases.

Rear Rotor Velocity

To mitigate the lack of information about the rear rotor velocity corresponding to the experimental data, the CFD validation case was run with different rear rotor angular velocities. Their descriptions and assigned letters (O,A-E) are given in Table 2. Their resulting CFD-calculated longitudinal forces, F_x, vertical forces, F_y, resulting thrusts, T, and moments, M, are given in Table 3. Each case presented in these tables has 3.2M cells and uses 750 timesteps per rotation. As an exception, the refined mesh case (E) has 4.7M cells, uses 3,000 timesteps per rotation, and takes more cycles to achieve periodic stability. All the force values shown in Table 3 are for the whole aircraft. The thrust averages are obtained by integrating the value at each timestep over a complete revolution.

Table 2: Definition of the validation cases.

case	description
O)	experimental data
A)	rear rotor retreating blades at 25 m/s
B)	rear rotor retreating blades at 12.5 m/s
C)	motionless rotor
D)	rear rotor retreating blades at 12.5 m/s in the negative direction
E)	motionless rotor with refined mesh

While none is able to accurately reproduce the longitudinal drag forces measured experimentally, the motionless rotor (C) gets closer

Table 3: Force results with the rear rotor at different angular velocities (A-E) compared to the experimental data (O).

	Fx	Fy	T	M
O)	0.612	1.00	-	-
A)	1.24	0.830	1.50	-0.489
B)	1.24	0.784	1.47	-0.570
C)	1.12	1.02	1.52	-0.591
D)	1.25	1.06	1.65	-0.598
E)	1.17	0.964	1.52	-0.657

to the experimental results of Fx and Fy. The refined mesh does not provide a closer match with experimental data, which confirms that the 3.2M-cell mesh is adequate. Unexpectedly, the total vertical forces decrease when the rear rotors rotate faster. To investigate this behavior, the forces generated by the two front rotors are extracted and shown in Table 4 while those generated by the two rear rotors are shown in Table 5.

Table 4: Front rotor force results for different rear-rotor angular velocities.

	Fx	Fy	T	M
A)	0.937	1.18	1.51	0.0411
B)	0.942	1.21	1.54	0.0422
C)	0.945	1.25	1.57	0.0418
D)	0.850	1.18	1.45	0.0368
E)	1.04	1.25	1.63	0.00516

Table 5: Rear rotor force results for different rear-rotor angular velocities.

	Fx	Fy	T	M
A)	0.480	-0.0318	0.484	-0.0174
B)	0.429	-0.210	0.479	-0.00365
C)	0.298	-0.0927	0.313	0.00278
D)	0.465	-0.234	0.522	0.0172
E)	0.342	-0.0677	0.350	0.00214

There are thus several explanations for the drop in vertical forces when the rear rotors rotate faster. When the rear rotor rotates at equivalent 12.5 m/s it generates a considerable downforce which represents the major contribution to the lift loss. The remaining loss is caused by a lower lift on the front rotor and a stronger downforce on the airframe. Diversely, when the rear rotor rotates at 25 m/s, the contribution to the lift loss is entirely caused by a loss of lift on the front rotor and a larger downforce on the airframe. This increased downforce is significantly due to the influence of the front rotor outflow. The rear rotor contributes more to drag than to lift, which is due to flying with hover parameters and incoming wind.

The results show near zero moments about the rear rotor, as expected for unpowered rotors. The front rotor has a relatively steady force output regardless of the behavior of the rear rotor. This is expected because the incoming wind pushes the outflow of the rear rotor away from the front rotor. The angle of the non-rotating rear rotor in the CFD simulations of cases C and E are equal and chosen arbitrarily as the configuration where blade 1 is at its topmost position. Further tests including other angular positions we not conducted, because the moment on the rear rotor is deemed small enough to indicate that it is in quasi-equilibrium. Also, the contributions of the rear rotor are smaller and thus less crucial for proper validation.

Flight Velocity

The capability of the model to follow the experimental trends at various forward flight velocities was also verified. Case C, having a standstill rear rotor and the unrefined mesh having 3.2M cells, was chosen as the baseline case for this further testing. The CFD and experimental forces obtained for the full aircraft at different flight velocities is shown in Figs. 4 and 5.
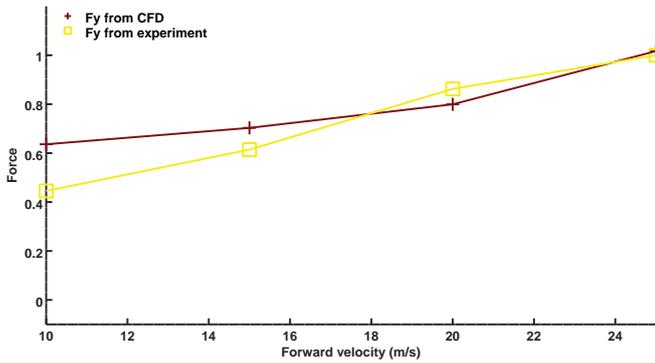
Figure 4: Trend match between simulation and experiment vertical force.
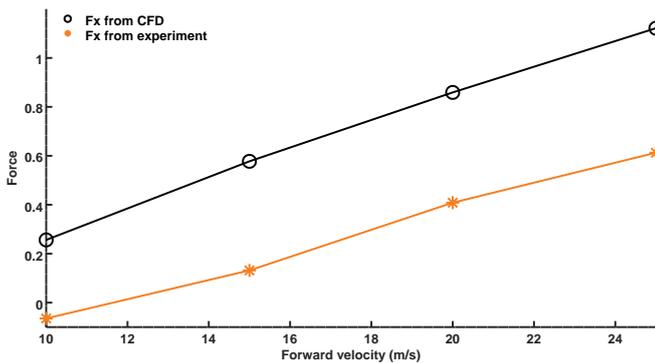
Figure 5: Trend match between simulation and experiment longitudinal force.

The results of Fig. 4 confirm that the CFD model adequately reproduces the vertical forces from the wind tunnel experiments at both low and high forward velocities. As for the prior tests, the longitudinal force comparison shown in Fig. 5 is not as good. However, they show a constant-value offset along the different tested velocities. This could indicate that the force scale used experimentally was calibrated to yield null forces at the lowest forward velocity. However, this assumption cannot be confirmed from the currently available experimental information. Regardless of this, the calculated longitudinal forces carefully follow the trend of the experimental data at various flight velocities. A mesh refinement study was undertaken prior to choosing to final mesh size and is reported with more details in the companion paper [35]. It covered both the airframe alone with grids having 0.3 to 1.7 million cells and the whole aircraft with grids having 3.7 to 5.7 million cells. It led to a slight refinement which was applied to the mesh. It allowed a better vortex resolution in zones away from the rotor blades. By avoiding changes in the mesh near the blades, the timestep did not need to be reduced. The final mesh is shown in Figs 6 to 8 and has 3.7M cells.

Cases Examined

This paper focuses on studying the respective impacts of the various possible configurations of the aircraft. Thus, starting from the reference case, which is very close to the wind tunnel model, 6 other cases were created during the study. Previous experimental tests showed that the efficiency of the current rotor is better with 6 blades and rotor sized endplates. The literature review also confirmed that 6 blades is a popular choice [2, 5, 36, 3]. Thus, the endplates geometry and the number of blades per rotor were unaltered during this study.

The baseline case is referred to as the *expLike* case. It is based on the 2014 wind tunnel experimental setup of the aircraft. The main difference with the experimental campaign is that both rotors of the *expLike* simulation are powered. The geometry and simulation parameters are those previously given in Table 1 with the exceptions
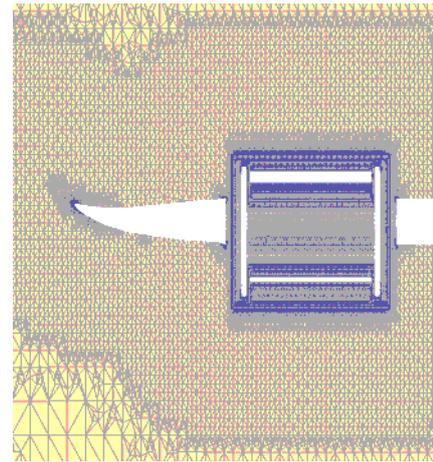
Figure 6: Final mesh's y-z plane showing a front rotor.
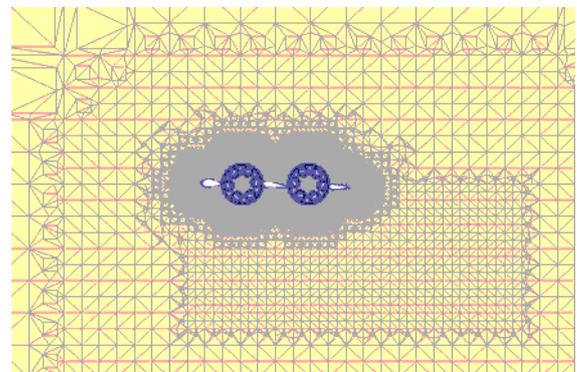
Figure 7: Final mesh's x-y plane view of the whole aircraft.
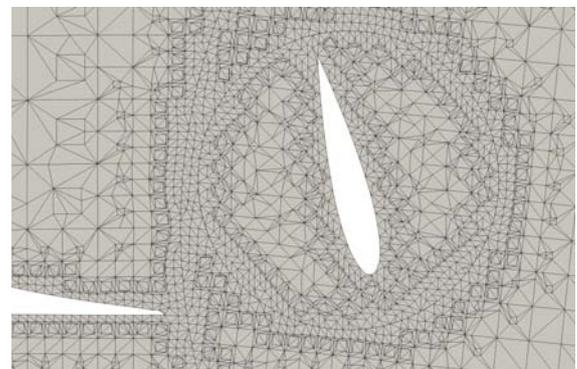
Figure 8: Final mesh's x-y plane. Rear rotor blade and the midwing on its left.

that the airframe has a forward velocity of 25 m/s and a null AoA, while the rotors have angular velocity of 3750 RPM. Every other examined case is a modification of this reference *expLike* case.

The airframe of the D-Dalus L1 has a wing shaped beam that lies along the spanwise axis in between the front and rear rotors. This beam is referred to as the midwing and is shown in Fig. 9. In order to understand its influence on the rotor outflow, that midwing is replaced by a 50 mm cylinder for the *expBeam* case.

Results

Figure 9 identifies the different parts of the aircraft that will be discussed. The figure is taken at a time of 0.099735s which

Table 6: Summary of the cases presented in this paper.

expLike	reference case
maxPitch	blade AoA range of [-46°, 44°]
hover	null forward velocity
rawHover	null forward velocity and no airframe
noBody	no airframe
expBeam	cylinder shaped midwing
noBodyUp	no airframe and rear rotors raised by half a rotor diameter

corresponds to 6.234 cycles and is the initial time for most plots presented. The position of blade 1 at that time, is seen in Fig. 9. The angles of the blades that are referred to in this paper were defined in Fig. 2, one should note that the polar coordinate systems of the front and rear rotors differ. All the force outputs given do, however, respect the global coordinate axes of Fig. 9. This means that Fx and Fy are always drag and lift, respectively. It is recalled that the results presented in this paper are all normalized. However, the zeros are unaltered from the reality are indicated on the plots by a blue line.
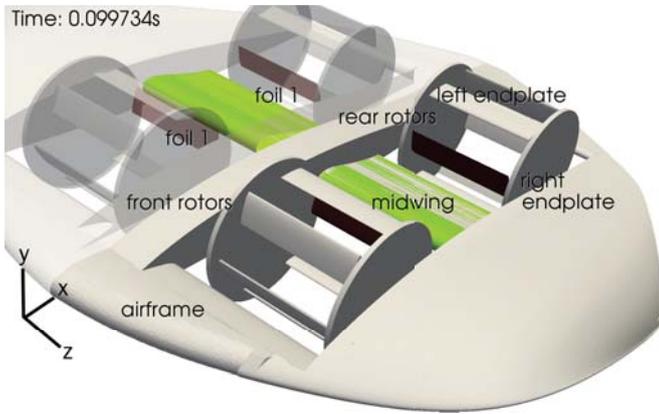
Figure 9: Identification of the different parts of the D-Dalus at time of 0.099734s or 6.234 cycles along with the reflected portion of the CFD simulation. Mid-wings in pale green and blade 1 (foil 1) of each rotor at 173° in dark red.

Video animations of APPENDIX B are referred to in the text but not essential for correct interpretation.

Table 7: Definition of the planes and depths used in this paper.

plane	description
x-y	side view with planes [0-6] equally spaced and going from the inner edge (0) of the rotor blade to its outer edge (6), along its span.
x-z	top view with planes [0-6] equally spaced and going from near the bottom (0) of the rotor to near its top (6), along the vertical axis.
y-z	front view with planes [0-6] equally spaced and going from the rear edge (0) of the airframe to its front edge (6), along the longitudinal axis.

Periodic Stability

Some insight on the periodic stability of the flow can be obtained from the CFD simulation. The output forces plotted over time were observed in order to gain a better understanding of how the flow stabilizes during the simulation. It was noticed that immediately after the first rotor cycle is completed the vertical forces on the individual blades of the rear rotor reach a stable pattern. Figure 10 demonstrates this by reporting the forces on blade 1 of the rear rotor. Due to their position behind both the airframe and the front rotor, rear rotor forces are the most perturbed ones. Thus, once they stabilize one can assume that the whole model reached stability. The same figure also shows

that the *hover* case stabilizes during the first cycles and shows a better periodic stability. This is an expected result as there is the absence of the incoming wind of the forward velocity. Consequently, this quick reaching of periodic stability is most obvious for the *rawHover*, as shown in Fig. 11. That figure presents the time evolution of the vertical force on the whole aircraft where each cycle going from the 2nd to the 6th are superposed. They are similar to each other right at the 2nd revolution of the rotor. The *expBeam* and *noBody* cases are no exception and also show disturbances on the rear rotor. As expected for forward flight, the forces on the front rotor reach periodic stability faster than those on the rear rotor.
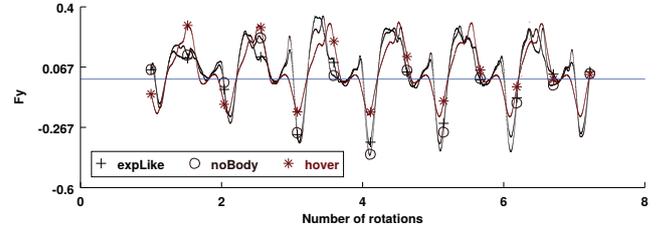
Figure 10: Vertical forces on blade 1 of the rear rotor plotted against the number of complete rotations of the rotor. Period going from 1 to 7.227 rotation cycles.
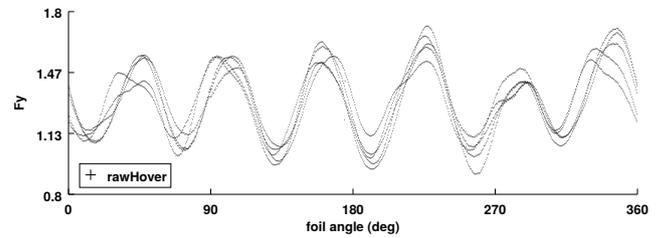
Figure 11: Vertical forces on the whole half aircraft multiplied by 2 plotted against the angle between the rear rotor's blade 1 arm and the positive x-axis. Period going from 2 to 7 rotation cycles.

It is also noted that even though being relatively stable, the wake of each case slowly continues to expand after 7 rotations. Even for a case as stable as *rawHover*, one can note that the wake continues to slowly expand in time. However, plotting the evolution of the solutions over a longer period of time confirms that the cases remain stable. This stability is visible in Fig. 12 where the lift generated by the first blade of the rear rotor of the *expLike* is shown up to the 15th cycle.
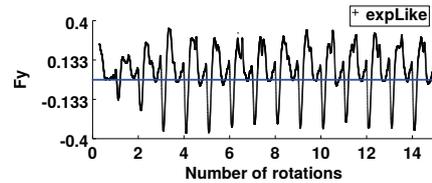
Figure 12: Vertical forces on blade 1 of the rear rotor: plotted against the number of complete rotations of the rotor. Period going from 0.3 to 15.3 rotation cycles.

Finally, the CFD simulations of [22] and [24] reach periodic stability after 3 and 7 rotations. Considering that and the results obtained, it was chosen that the forces were stable enough to be analyzed both quantitatively and qualitatively after 6.234 cycles. The solution of each case studied was nonetheless inspected over time to ensure it had reached periodic stability.

Baseline Case

In agreement with the research of [11], the simulated flow of the *expLike* case exhibits an important 3D behavior, as seen in Fig. 13. The flow is asymmetric about the rotor midpoint along the spanwise

axis. This is due to the shape of the airframe and to the rotors being placed side-by-side in groups of two. Vorticity is stronger at the tips of the blades, and this effect is more pronounced for the hover scenarios. This can be seen in Videos 4 and 5. Near the tips of the blades the vorticity, pressure, and velocity fields are more chaotic. This is likely due to the interaction between the endplates and the rotor. The low-pressure zone that occurs on the blade coming up from its lowest position is larger at midspan of the blades than at their tips for each of the 7 cases. When in forward flight, these low pressure zones widen for the blades going upstream and almost disappear for the blades going downstream. These low pressure zones also increase with the maximum blade pitch angle, as seen in Video 1. Disturbances are also present in the vicinity of the airframe, as seen in Figs 13 and 15 and Video 6. This effect is minor for pressure.

(a) y-z plane.

(b) x-z plane.

(c) x-y plane.

Figure 13: Vorticity fields of the wake of the *expLike* case at t=0.099734s.

For the *expLike* case, the wake of the front rotor merges quickly with that of the rear rotor while those of the side-by-side rotors remain separate, as seen in Fig. 13. Vortices are created by the endplates in forward flight, as seen on Fig. 14 which shows the case without airframe to isolate the endplate effect. The figure shows that the endplate wakes created by the rear rotor are partially absorbed back into the rotor. It should be noted that such reabsorption occurs for all cases in forward flight.

Flow interaction between the blades of the same rotor is most important at the location of peak forces. This can be seen for the rotors of Figs 13(c) and 21(a) which show blades colliding into disturbances and Figs 23 and 24 which show large force magnitudes. This agrees with the forward flight findings of [11]. The quasi-sinusoidal pitching function limits lift generation of each blade to roughly a sixth of the rotation. This is seen in Fig 10 which shows that the lift forces of a blade reach a magnitude able to counter the negative lifts from the other blades for roughly a sixth of its rotation.

Figure 14: Vorticity of the *noBody* case at x-z plane at 4/6 and t=0.108647s. Rear rotor in the center.
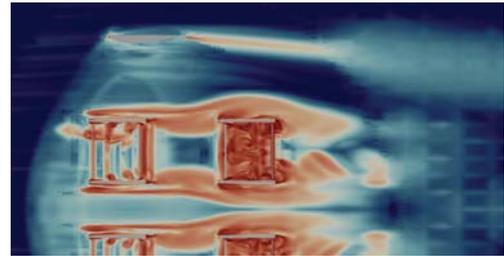
(a) *expLike*.
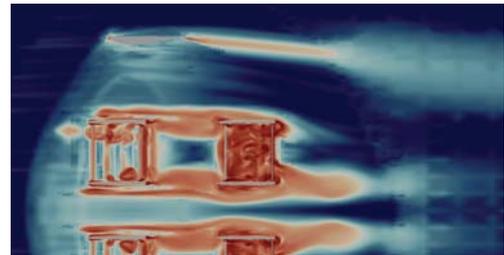
(b) *expBeam*.
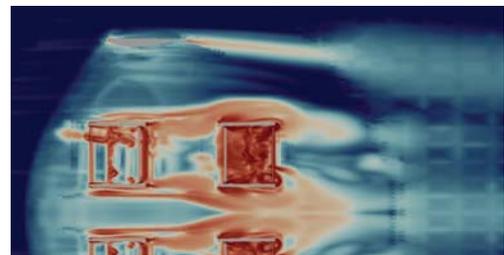
(c) *maxPitch*.

(d) *hover*.

Figure 15: Vorticity at the fifth x-z planes at t=0.114545s.

Thrust Phase

On the front rotor, the different cases have force outputs with different phases. This is seen in Fig. 23. The *maxPitch* case has an early force output while the *hover* and *rawHover* cases lag behind the other cases. Figure 24 shows that the peak force phases on the rear rotor

coincide better with each other and that their overall response is noisier. The peak forces lag corresponds with the findings of [24]. The two figures show that the blades of both rotors generate lift when in the bottom half of their cycle. When going from their topmost position at $90°$ to their horizontal position at $180°$, lift is only generated by the blades of the front rotor which are in forward flight. The magnitude of this lift is small. The negative lift generated in that zone by the blades of the rotors in hover may be caused by the rapid pitching of the blade. The forward flight velocity counters this effect by causing a sail effect on the blade. This sail effect is clearly visible in Fig. 21 where the front rotor blades of the cases in forward flight exhibit vortices downwind in the zone between $90°$ and $180°$. The individual blade forces of Figs. 23 and 24 confirm the findings of [24] who found that the instantaneous magnitude and direction of the thrust produced by the cycloidal rotor vary significantly over a cycle.

Forward Flight

The aircraft generates twice as much lift when in forward flight than when in hover. The front rotor vertical forces are doubled while the rear rotor forces remain almost intact. Half of this lift increase comes from the airframe while the other half comes from the front rotor. The rear rotor produces fairly constant lifts for all cases studied and both front and rear rotors generate considerably more drag when in forward flight.

The influence of the forward velocity on the AoA of the rear rotor blades is given in Table 8 for which the associated blade conditions a, b, c, and d are pictured in Fig. 16. Induced flow, rotor interaction, dynamic effects, and discontinuity that occurs when the AoA reaches $180°$ are neglected. Applying these conditions to a rotor with a blade pitching function equal to that of the *expLike* case gives an increasing AoA for $[271°,32°]$ and $[91°,165°]$ on the front rotor and for $[33°,89°]$ and $[166°,270°]$ on the rear rotor. For the remaining angles, the AoA decreases. These ranges were depicted on the rotors of Fig. 2. Accordingly, these zones match the ranges of increased and decreased thrust seen in Figs 23 and 24 when comparing the *explike* case the *hover* case. With the stronger pitching of the *maxPitch* case, the zones of increased AoA slightly change to become $[271°,43°]$ and $[91°,163°]$ for the front rotor and $[44°,89°]$ and $[164°,270°]$ for the rear rotor.

Table 8: Impact of the forward velocity on the AoA of the rear rotor.

	blade vel. w.r.t. wind vel.	blade nose angle w.r.t. x-axis	effect on rear rotor AoA
a	$]0°,180°[$	$]270°,90°[$	decreases
b	$]180°,360°[$	$]270°,90°[$	increases
c	$]0°,180°[$	$]90°,270°[$	increases
d	$]180°,360°[$	$]90°,270°[$	decreases
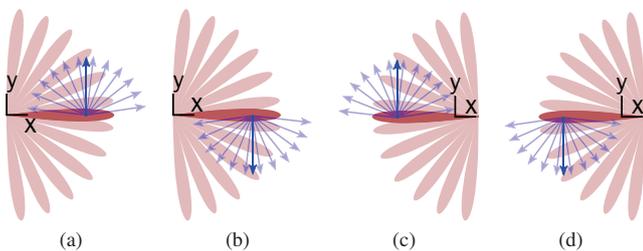
Figure 16: Cases from Table 8 for a wind coming from the negative x-axis. Ranges of blade positions and velocities covered are shown by red airfoils and blue arrows, respectively.

These increases in AoA make cases with forward velocity take more time to reach periodic stability because the top blade of their rear rotors reaches very high AoA. Furthermore, every second blade creates a strong vortex which is broken apart by the following blade.

The expelled portion of the vortex is quickly reabsorbed by the rotor and collides more times into its blades. This can be seen in Fig. 21 and Video 1. Figs. 25 and 26 also confirm that the rear rotor generates more chaotic lift forces. While stronger vortices do lie inside both rotors in forward flight, vortex shedding on the front rotor occurs at the bottom of the rotor. Thus vortex impact is limited to the blade that follows. The increased vorticity zones on both front and rear rotors correspond to those identified analytically for increased AoA.

The flow fields near the top of the front rotor, thus where the blades travel in the direction of the wind, are similar to those in hover. The increased lift is not produced by the blades before having crossed the top zone. Rather, the lift is concentrated in the bottommost zone of the front rotor, around $270°$. The incoming wind reduces the front rotor blade's AoA before it reaches the top and increases it after. Nevertheless, the lift from the front rotor blades is positive over the whole cycle. As shown in Fig. 24, the rear rotor blades have a negative lift zone after the topmost position which is likely due to the pitching motion of the blades themselves. That same pitching effect is suspected to influence both front and rear rotor blades in hover to create a negative lift between $[80°,160°]$.

These findings indicate that an adjusted pitching schedule on the rear rotor would increase its efficiency. By doing so, one can expect to obtain vertical forces and power consumption approaching those of the front rotor. This would be a considerable benefit since the front rotor produces far more thrust when in forward flight than when in hover.

Hover

In hover, the thrust generation lasts longer and has a weaker peak. As expected for the *rawHover* case, the blades of the front and rear rotors have equal but inverted moments about both their blade's pivot axis and their rotor's axis. Also, Fig. 27 showed that *hover* has the smallest airframe lift. As expected, drag and moment are negligible. The very small drag force comes exclusively from the airframe and is due to its asymmetric shape. Figure 27 shows that the thrust generated by the aircraft in hover with the modified midwing is steadier. Fig. 22 shows that both hover cases have minimal rotor interaction. Fig. 21 shows that the wakes of the hover cases front and rear rotors tend to remain separated longer. These effects can also be seen in Video 2.

The results also confirm the findings of [24] that the cycloidal rotor induces a flow deflection which is unique to such rotors. This effect is explained by the multiple encounters that the stream has with the blades. Hence, it is only seen in the x-y plane, as in Fig. 21 for the hover cases. The y-z and x-z planes show a wake that sheds vortices and narrows as it gets further away from the aircraft, as seen in Fig. 18 and Video 3. This narrowing effect is also noted by [37]. At midspan of the very simple *rawHover* case, the flow is most stable and shows rotor inflow and outflow very similar to the visualization done with a high-speed camera and to those reported by [3].

Also, it is widely known that helicopter rotors create tip vortices [38]. It is thus no surprise to see them appear on the tips of the blades. They are quickly absorbed by the induced flow, as seen in Fig. 17. However, these tip vortices might not be present on the physical aircraft because of friction effects in the space between the blade tips and the endplates. Small disturbances appear near the airframe of the *hover* case and become negligible when distancing the rotors.

Figures 23 and 24 show that Fx is different for the blades going up than for those going down, as was advanced by [24]. This can be seen when taking into consideration the phase of the pitch function and thus reading the force $37.5°$ before the horizontal position. This difference is partly due to the induced flow which changes its impact according to the direction of the blade. Also, the blades of the front and rear rotors that meet at the center of the aircraft push away from each other. This is also the case $37.5°$ before meeting, where they
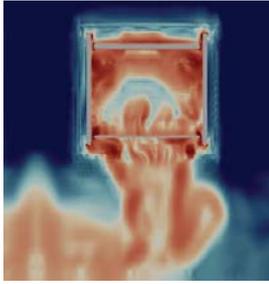
Figure 17: Vorticity fields showing the tip vortices of the *rawHover* case at y-z plane at 2/6 and t=0.113443s.

(a) Front rotor, second y-z plane.
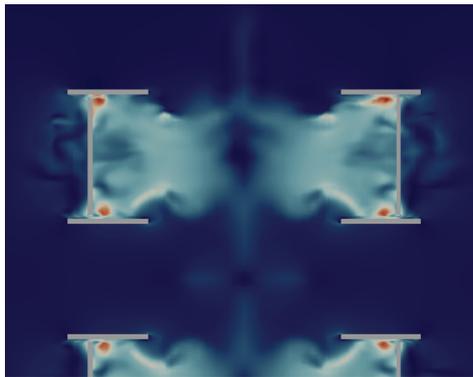
(b) Zeroth x-z plane.

(c) Third x-y plane.

Figure 18: Velocity fields of the *rawHover* case at t=0.104998s in diverse planes.

have a null local pitch angle. Finally, the dynamic pitching further complicates this phenomenon.

Large Pitching

Every case studied had a sinusoidal pitching schedule with 36° magnitude, -1° offset, and 37.5° phase. The exception is the *maxPitch* case which is a copy of the *expLike* case with a 45° pitch magnitude. That change surprisingly has a negligible effect on the drag and lift of the whole aircraft. The lifts increase on both front and rear rotors by roughly 6-10% while airframe lift nearly disappears. This is explained by a lower pressure under the leading edges of the midwing and under the airframe behind the rear rotor. A higher pressure above that last leading edge of the airframe further contributes to the lift reduction, as seen in Video 1. The rear rotor still produces only half the lift of the front rotor. Figures 23 and 24 show that the peak-to-peak amplitude of the thrust increases with the pitch angle. The power required by the *maxPitch* case is roughly 65% more than for the other cases. The mean power doubles for the front rotor and increases by 50% for the rear rotor. This is also seen when looking directly at the blade moments in Figs 23 and 24. Figures 25 and 26 highlight that a greater pitch function magnitude causes a growth in the maximum instantaneous power demand. The main difference with *expLike* is that the flow inside the rotors of *maxPitch* has higher velocities. This can be seen in Fig. 21 and Video 2.

Airframe and Midwing

The effects of the airframe are critical to the flow on the aircraft. For the baseline *expLike* case, a high pressure bubble gets pushed on the midwing by the descending blades of the rear rotor, as shown in Fig. 22(a) and Video 1. For *expBeam*, the flow induced by both rotors passes through smoothly, creating only a small vortex behind the tube, as in Fig. 22(e). In *noBody* the flow passes undisturbed, as seen in Fig. 22(d). These improvements apply mostly in forward flight. In hover, midwing obstruction and airframe interaction are almost null, as seen in Fig. 22(b). The effects aforementioned can also be seen in Video 2.

The airframe in hovering flight has a very small influence on the force output and power required by the rotors. Figure 27 indicates that, as expected, the airframe in hover has a nearly null moment about its center for the whole rotation cycle. It does, however, contribute negatively to lift and thus the *rawHover* case has a better mean lift.

When no airframe is present in forward flight, both rotors cause more drag and require more power. The front rotor generates more lift while the rear rotor generates less lift. Both rotors of the *noBody* case have better lift forces than the *expBeam* case, but total lift is smaller because of the absence of airframe lift. Substituting the midwing by a tube decreases the lift on the rear rotor and increases it on the front rotor. Figure 27 and the mean forces show that the increased lift of the *expBeam* originates mainly from the greater airframe lift. The influence of the airframe is considerable on the rear rotor in forward flight, as seen when comparing the Fy of the *expLike* and *noBody* cases in Figs 25 and 26. However, presence or absence of the airframe has a limited influence on the important repercussions of the forward velocity on the rear rotor. This can be seen by comparing *expLike*, *noBody*, *hover*, and *rawHover* in Video 2.

The airframe moments are negative for the cases in forward flight and strongest for the *expBeam* case. That case also has a airframe lift 50% stronger than that on the airframe of the *expLike*. This is due to the absence of blockage to the outflow of the front rotor and underlines the importance of proper midwing design.

Raising the Rear Rotor

The *noBodyUp* case consumes less power, causes less drag, and generates more lift than the *noBody*. These benefits come mainly from the rear rotor, even though it exhibits a similar flow as when leveled with the front rotor, as seen in Figs. 21(e) and 21(f). Both rotors require less power and the front rotor endplate vortices influence on

the rear rotor is minimized, as seen in Fig. 19. The *noBodyUp* case further confirms that the rear rotor's more chaotic state is mostly caused by the forward velocity, as seen by the vortices visible in Fig. 21(f) in the bottom portion of the cycle for the front and in the top portion for the rear rotors. Figure 20 further shows that the flow on the top blades of the rear rotor, even when moved up, is still disturbed when compared to the equivalent case in hover.

(a) *noBody* case.

(b) *noBodyUp* case.
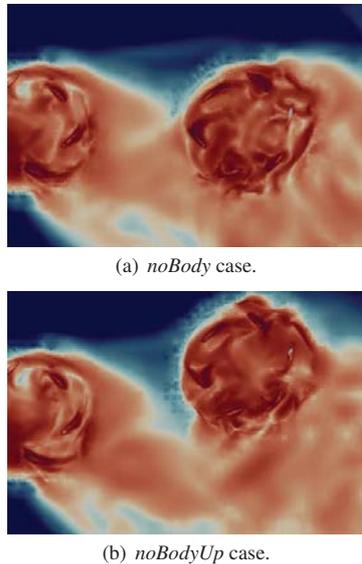
Figure 19: Visualization of the interaction between the front rotor endplates and the rear rotor with the zeroth x-y plane vorticity fields at t=0.111364s.

(a) *rawHover* case.

(b) *noBody* case.

(c) *noBodyUp* case.
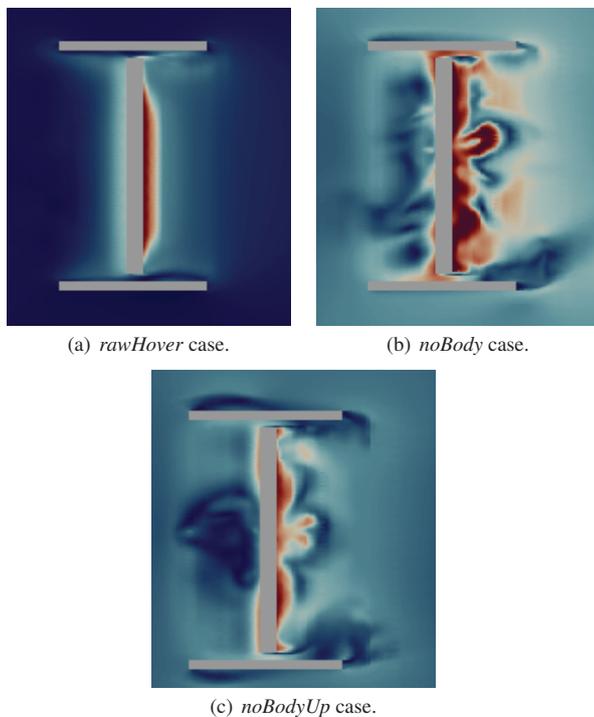
Figure 20: Velocity fields near the rear rotor's top blade on the sixth x-z plane, adjusted for *noBodyUp*, at t=0.114589s.

Discussion

The option of modeling the endplates as a porous zone within the flow domain had initially been considered, to simplify the mesh near the AMI. The approach was, however, not retained because a boundary layer usually forms around a porous zone [39] and would have complexified the flow solution more than a slip wall and an endplate together. An aspect that was not investigated is the angular position of the non-rotating rear rotors, which, however, has an influence on the validation results. The influence of the most refined mesh (E) on the forces of interest was small and thus justified not using it. In all cases, the Fy and Fx forces on the endplates were minimal. Finally, approximating the flow as non-viscous and laminar does limit the level of precision of the simulation.

The comparison of the analytic AoA analysis with the CFD results made it clear that a simple analysis is able to predict the influence of pitch control and incoming flow modifications on the thrust tendency. This thus indicates that, in forward flight, the rear rotor could be made as efficient as the front one. Furthermore, in the ideal case, the pitch angle of each blade would vary according to any chosen mathematical function. Such a pitch control would increase the rotor efficiency and reduce thrust oscillations. Consequently, the smoother thrust would also reduce the required number of blades. As a confirmation, significant performance improvements on cycloidal rotors with individual pitch control were also shown by [14].

The vertical force is better correlated to the experimental measurements than the longitudinal force, as was reported by [27]. The vortices jumping from one blade to the consecutive one observed by [24] is also seen in the simulations of this study. The findings of [24] about the presence of large periodic variations in thrust and power and about the difference between the position of maximum thrust and maximum blade pitch angle are also confirmed by the present work.

Finally, the model was developed with repeatability in mind. It is thus set up to allow running a series of modifications on the geometry, pitching schedule, and attitude of the aircraft. Running one case on a recent computer using 4 cores takes one day per rotor cycle. Roughly 7 rotations are required to create stable output. It is thus reasonable to plan a turnover time of 10 days per case. To reproduce the model, the reader is encouraged to read the relevant publication [35].

Conclusion

This work on a cycloidal rotor aircraft showed the effects of dynamic pitching, the presence of vortices inside the rotor, and the complexity of the flow towards the endplates. It also showed that the flow in forward flight exhibits 3D perturbations even at midspan. These effects and the virtual camber are burdensome to model without 3D CFD, even with the most complex 2D analytical and numerical models. For example, the double streamtube model [3, 40, 41, 10], which is arguably the most accurate cycloidal rotor induced flow model currently in use, does not take them into consideration.

For all cases, a correlation was found between power required and the lateral forces on the endplates. This confirms that the power required by the rotors is proportional to the flow strength inside of them. It also indicates potential for lateral movement, were the endplates able to morph. The interaction between the two rotors was confirmed, but found to be less important than airframe interaction. The airframe may either reduce drag or cause blockage, depending on the different configurations studied.

With respect to the baseline case, the *maxPitch* case somewhat increases mean drag and lift. It drastically increases force peaks and the strength of the outflow from the rotors. It also reduces airframe efficiency and considerably increases power demand. The case in

hover has the weakest interference with the airframe, has front and rear rotors that behave equally, and has no endplate wake. A properly tuned forward flight case could avoid airframe interaction. The cleanest flow is obtained while in hover and without airframe. When no airframe is present, the total drag and power drawn by the rotors increases. Changing the midwing design increases the aerodynamic efficiency by reducing airframe interference. Finally, moving the rear rotor up also increases efficiency, but maintains a highly disturbed rear rotor flow because of the forward flight velocity.

Recommendation

From the conclusions, the following recommendations are issued to those who consider building a cyclogiro aircraft: evaluate the sail effect of the blades when performing forward flight and attempt to achieve the best lift to drag and power ratio; attempt to reduce the blockage caused by the endplates, and by the rotors, when in forward flight; avoid sending disturbed flow to the rear rotor; evaluate the interaction of the airframe with the rotor flow for both stationary and high-speed flight; consider the impacts the blades of different rotors have when pushing flow against each other; verify that the phase of the pitch function is properly adapted to each expected flight conditions; and, attempt to limit the pitch angles according to efficiency.

References

1. R. Gibbens, J. Boschma, and C. Sullivan, "Construction and testing of a new aircraft cycloidal propeller," in *Proceedings of 13th Lighter-Than-Air Systems Technology Conference.*, June 28-July 1 1999.

2. R. Gibbens, "Improvements in Airship Control Using Vertical Axis Propellers," in *Proceedings of AIAA's 3rd Annual Aviation Technology, Integration, and Operations (ATIO) Forum*, November 17-19 2003.

3. C. Y. Yun, I. K. Park, H. Y. Lee, J. S. Jung, and I. S. H., "Design of a New Unmanned Aerial Vehicle Cyclocopter," *Journal of the American Helicopter Society*, vol. 52, no. 1, 2007.

4. G. Ilieva, J. C. Páscoa, A. Dumas, and M. Trancossi, "A critical review of propulsion concepts for modern airships," *Central European Journal of Engineering*, vol. 2, no. 2, pp. 189–200, 2012. doi:10.2478/s13531-011-0070-1.

5. M. L. McNabb, "Development of a Cycloidal Propulsion Computer Model and Comparison with Experiment," Master's thesis, Mississippi State University, 2001.

6. C. M. Xisto, J. C. Páscoa, J. A. Leger, P. Masarati, G. Quaranta, M. Morandini, L. Gagnon, D. Wills, and M. Schwaiger, "Numerical modelling of geometrical effects in the performance of a cycloidal rotor," in *6th European Conference on Computational Fluid Dynamics*, (Barcelona, Spain), 20 - 25 July 2014.

7. J. A. Leger, J. C. Páscoa, and C. M. Xisto, "Aerodynamic optimization of cyclorotors," *J. of Aircraft Engineering and Aerospace Technology*, 2016.

8. M. Benedict, M. Ramasamy, I. Chopra, and J. G. Leishman, "Experiments on the Optimization of MAV-Scale Cycloidal Rotor Characteristics Towards Improving Their Aerodynamic Performance," in *American Helicopter SocietyInternational Specialist Meeting on Unmanned Rotorcraft*, (Phoenix, Arizona), January 20–22 2009.

9. M. Benedict, M. Ramasamy, I. Chopra, and J. G. Leishman, "Performance of a Cycloidal Rotor Concept for Micro Air Vehicle Applications," *Journal of the American Helicopter Society*, vol. 55, no. 2, pp. 022002–1–14, 2010. doi:10.4050/JAHS.55.022002.

10. M. Benedict, M. Mattaboni, I. Chopra, and P. Masarati, "Aeroelastic Analysis of a Micro-Air-Vehicle-Scale Cycloidal Rotor," *AIAA Journal*, vol. 49, no. 11, pp. 2430–2443, 2011. doi:10.2514/1.J050756.

11. A. H. Lind, T. Jarugumilli, M. Benedict, V. K. Lakshminarayan, A. R. Jones, and I. Chopra, "Flow field studies on a micro-air-vehicle-scale cycloidal rotor in forward flight," *Experiments in Fluids*, vol. 55, no. 12, 2014.

12. C. Barrass, "Chapter 22 - improvements in propeller performance," in *Ship Design and Performance for Masters and Mates* (C. Barrass, ed.), pp. 218 – 227, Oxford: Butterworth-Heinemann, 2004.

13. G. J. M. Darrieus, "Turbine having its rotating shaft transverse to the flow of the current," Dec. 8 1931. US Patent 1,835,018.

14. I. S. Hwang, H. Y. Lee, and S. J. Kim, "Optimization of cycloidal water turbine and the performance improvement by individual blade control," *Applied Energy*, vol. 86, no. 9, pp. 1532–1540, 2009.

15. M. El-Samanoudy, A. A. E. Ghorab, and S. Z. Youssef, "Effect of some design parameters on the performance of a Giromill vertical axis wind turbine," *Ain Shams Engineering Journal*, vol. 1, no. 1, pp. 85–95, 2010.

16. T. Maître, E. Amet, and C. Pellone, "Modeling of the flow in a Darrieus water turbine: Wall grid refinement analysis and comparison with experiments," *Renewable Energy*, vol. 51, pp. 497–512, 2013.

17. M. Schwaiger and D. Wills, "D-Dalus VTOL – efficiency increase in forward flight," *Aircraft Engineering and Aerospace Technology*, vol. 88, no. 5, pp. 594–604, 2016.

18. M. Schwaiger, "Aircraft," tech. rep., US Patent 7735773 B2, 2010.

19. M. Schwaiger, "Airplane," tech. rep., US Patent USD709430 S1, 2014.

20. J. Páscoa, "Final Report - CROP (Cycloidal Rotor Optimized for Propulsion)," tech. rep., European Comission, 2015.

21. G. Iosilevskii and Y. Levy, "Aerodynamics of the cyclogiro," in *Proceedings of the 33rd AIAA Fluid Dynamics Conference and Exhibit*, (Orlando, Florida), 23-26 June 2003.

22. G. Iosilevskii and Y. Levy, "Experimental and Numerical Study of Cyclogiro Aerodynamics ," *AIAAJ*, vol. 44, no. 12, 2006.

23. J. Seifert, "Aerodynamic Analysis of a new Hybrid Rotor," in *Proceedings of Deutscher Luft und Raumfahrt Kongress*, (Aachen, Germany), 2009.

24. J. Tang, Y. Hu, and B. Song, "Investigation on the unsteady aerodynamics of cycloidal propeller in hovering flight," in *Proceedings of the Institution of Mechanical Engineers, Part G: Journal of Aerospace Engineering*, vol. 229:13, (Phoenix, Arizona), pp. 2519–2536, November 2015.

25. Y. Wang, X. Sun, B. Zhu, H. Zhang, and D. Huang, "Effect of blade vortex interaction on performance of darrieus-type cross flow marine current turbine," *Renewable Energy*, vol. 86, pp. 316 – 323, 2016.

26. Y. Hu, F. Du, and H. L. Zhang, "Investigation of unsteady aerodynamics effects in cycloidal rotor using RANS solver," *The Aeronautical Journal*, vol. 120, pp. 956–970, may 2016.

27. K. Yang, "Aerodynamic analysis of an mav-scale cycloidal rotor system using a structured overset rans solver," Master's thesis, University of Maryland at College Park, 2010.

28. A. Alaimo, A. Esposito, A. Messineo, C. Orlando, and D. Tumino, "3d cfd analysis of a vertical axis wind turbine," *Energies*, vol. 8, no. 4, p. 3013, 2015.

29. M. Benedict, T. Jarugumilli, and I. Chopra, "Effect of Rotor Geometry and Blade Kinematics on Cycloidal Rotor Hover Performance," *Journal of Aircraft*, vol. 50, no. 5, pp. 1340–1352, 2013. doi:10.2514/1.C031461.

30. L. Gagnon, M. Morandini, G. Quaranta, V. Muscarello, and P. Masarati, "Aerodynamic models for cycloidal rotor analysis," *AEAT*, vol. 88, no. 2, pp. 215 – 231, 2016. doi:10.1108/AEAT-02-2015-0047.

31. "Cycloidal rotor optimized for propulsion." http://crop.ubi.pt. Last accessed 9 October 2018, (Archived by WebCite® at http://www.webcitation.org/732J2ltuX).

32. L. Gagnon, M. Morandini, G. Quaranta, V. Muscarello, G. Bindolino, and P. Masarati, "Cyclogyro Thrust Vectoring for Anti-Torque and Control of Helicopters," in *AHS 70th Annual Forum*, (Montréal, Canada), May 20-22 2014.

33. "Dynamic mesh within a dynamic mesh." https://www.cfd-online.com/Forums/openfoam-solving/124586-dynamic-mesh-within-dynamic-mesh.html. Last accessed 9 October 2018, (Archived by WebCite® at http://www.webcitation.org/732Iacm0Y).

34. "Free slip moving wall BC." https://www.cfd-online.com/Forums/openfoam-solving/105274-free-slip-moving-wall-bc.html#post509989. Last accessed 9 October 2018, (Archived by WebCite® at http://www.webcitation.org/732Ixxfzg).

35. L. Gagnon, G. Quaranta, and M. Schwaiger, "Open Source 3D CFD of a Quadrotor Cyclogyro Aircraft," in *under review by 11th OpenFOAM Workshop Book* (J. M. Nóbrega and H. Jasak, eds.), Springer International Publishing AG, 2017.

36. J. Sirohi, E. Parsons, and I. Chopra, "Hover performance of a cycloidal rotor for a micro air vehicle," *Journal of the American Helicopter Society*, vol. 52, no. 3, pp. 263 – 279, 2007.

37. C. H. Lee, S. Yong Min, J. E. Lee, and S. J. Kim, "Design, analysis, and experimental investigation of a cyclocopter with two rotors," *Journal of Aircraft*, 2016.

38. A. Brocklehurst and G. Barakos, "A review of helicopter rotor blade tip shapes," *Progress in Aerospace Sciences*, vol. 56, pp. 35 – 74, 2013.

39. W. P. Breugem, B. J. Boersma, and R. E. Uittenbogaard, "The Laminar Boundary Layer over a Permeable Wall," *Transport in Porous Media*, vol. 59, pp. 267–300, June 2005.

40. E. Parsons, "Investigation and Characterization of a Cycloidal Rotor for Application to a Micro-Air Vehicle," Master's thesis, University of Maryland, 2005.

41. I. Paraschivoiu, O. Trifu, and F. Saeed, "H-darrieus wind turbine with blade pitch control," *International Journal of Rotating Machinery*, vol. 2009, 2009.

Contact Information

Louis Gagnon, Ph.D.
Louis.Gagnon@Polimi.it

Acknowledgments

Definitions, Acronyms, Abbreviations

AoA	Angle of Attack
AMI	Arbitrary Mesh Interface
CFD	Computational Fluid Dynamics
midwing	Wing shaped beam located along the spanwise axis between the front and rear rotors
RANS	Reynolds-averaged Navier–Stokes

APPENDIX A

This section presents figures that occupy too much space to include in the main text. Plots of the periodically converged force outputs on selected components of the aircraft are presented in Figs 23 to 27. The jump visible on these plots when blade 1 is at 173° is caused by the plotting cycle starting at that angle. For blade 1, plots in Figs 23 and 24 give the drag Fx; the lift Fy; the thrust in the x-y plane T; the moment about the rotor center; and the torsional moment Mf about the blade pivoting axis. The equivalent data for the front and rear full rotors are given in Figs 25 and 26, respectively. Finally, the forces on the airframe are shown in Fig. 27.

(a) *expLike*.

(b) *maxPitch*.

(c) *hover*.

(d) *rawHover*.

(e) *noBody*.

(f) *noBodyUp*.
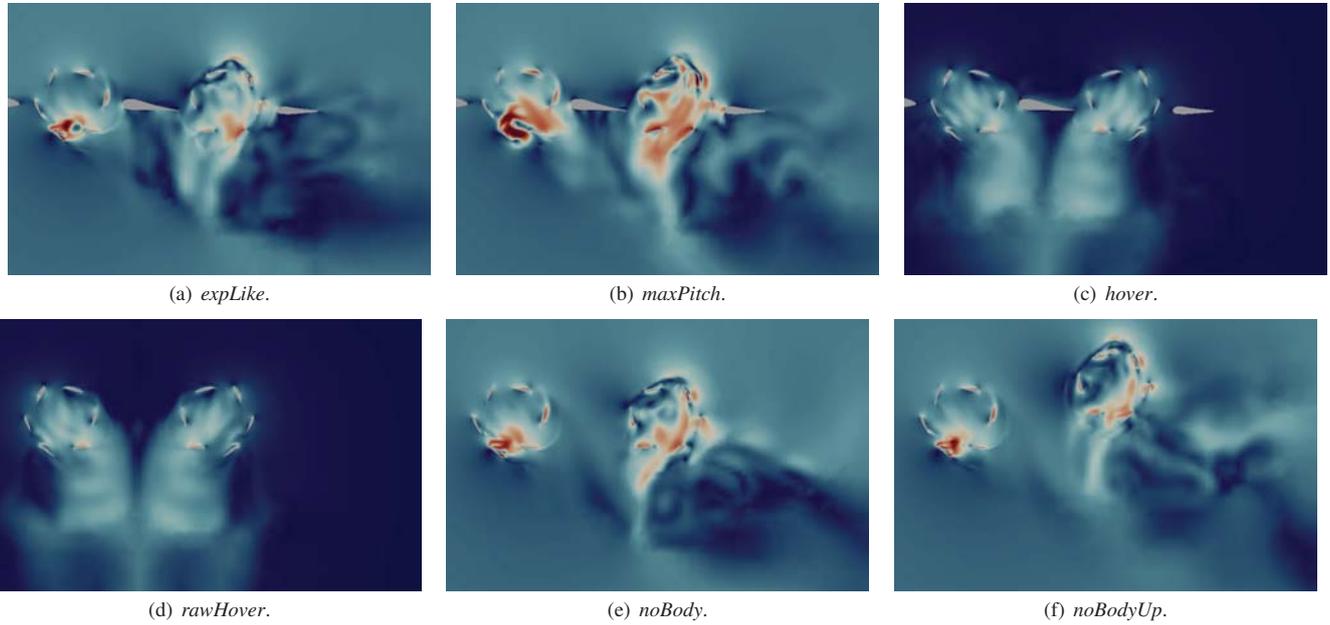
Figure 21: Velocity fields at t=0.113104s on the x-y plane at midspan. Front of the aircraft is on the left.

(a) *expLike*.

(b) *hover*.

(c) *rawHover*.

(d) *noBody*.

(e) *expBeam*.
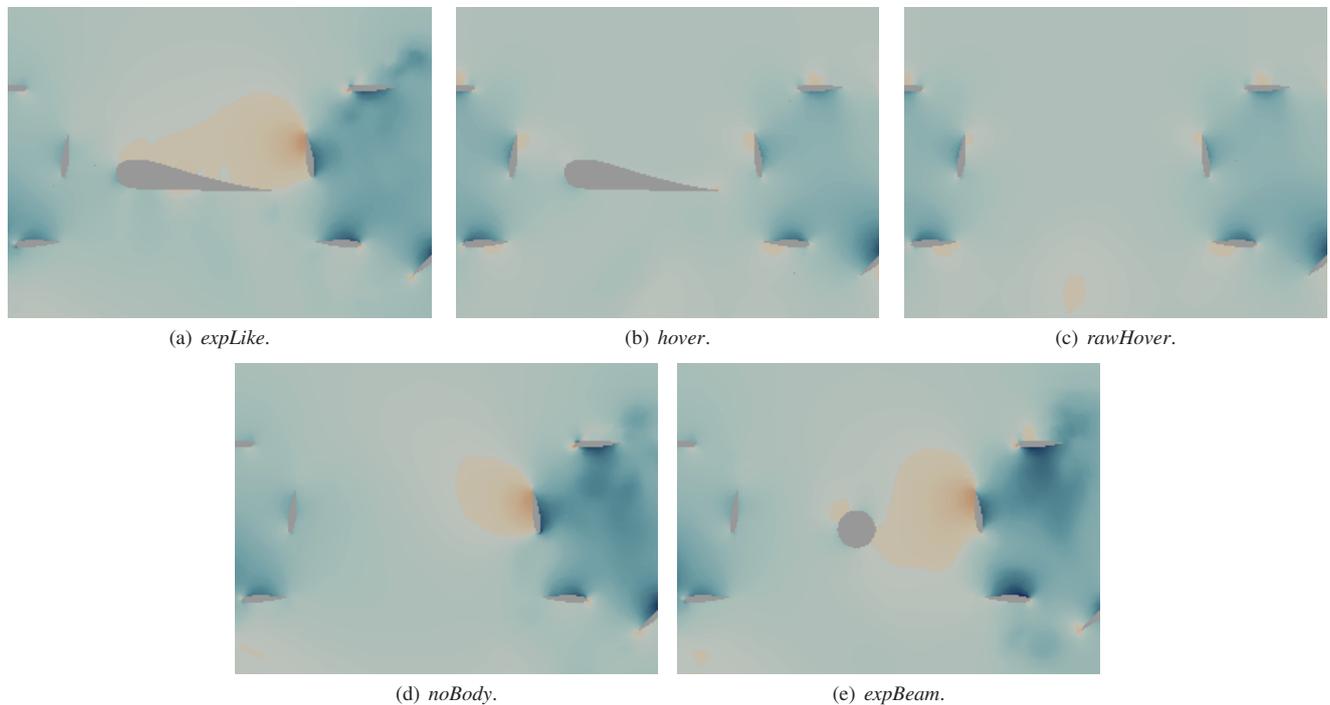
Figure 22: Pressure fields between front and rear rotors at t=0.11289s on the x-y plane at midspan.
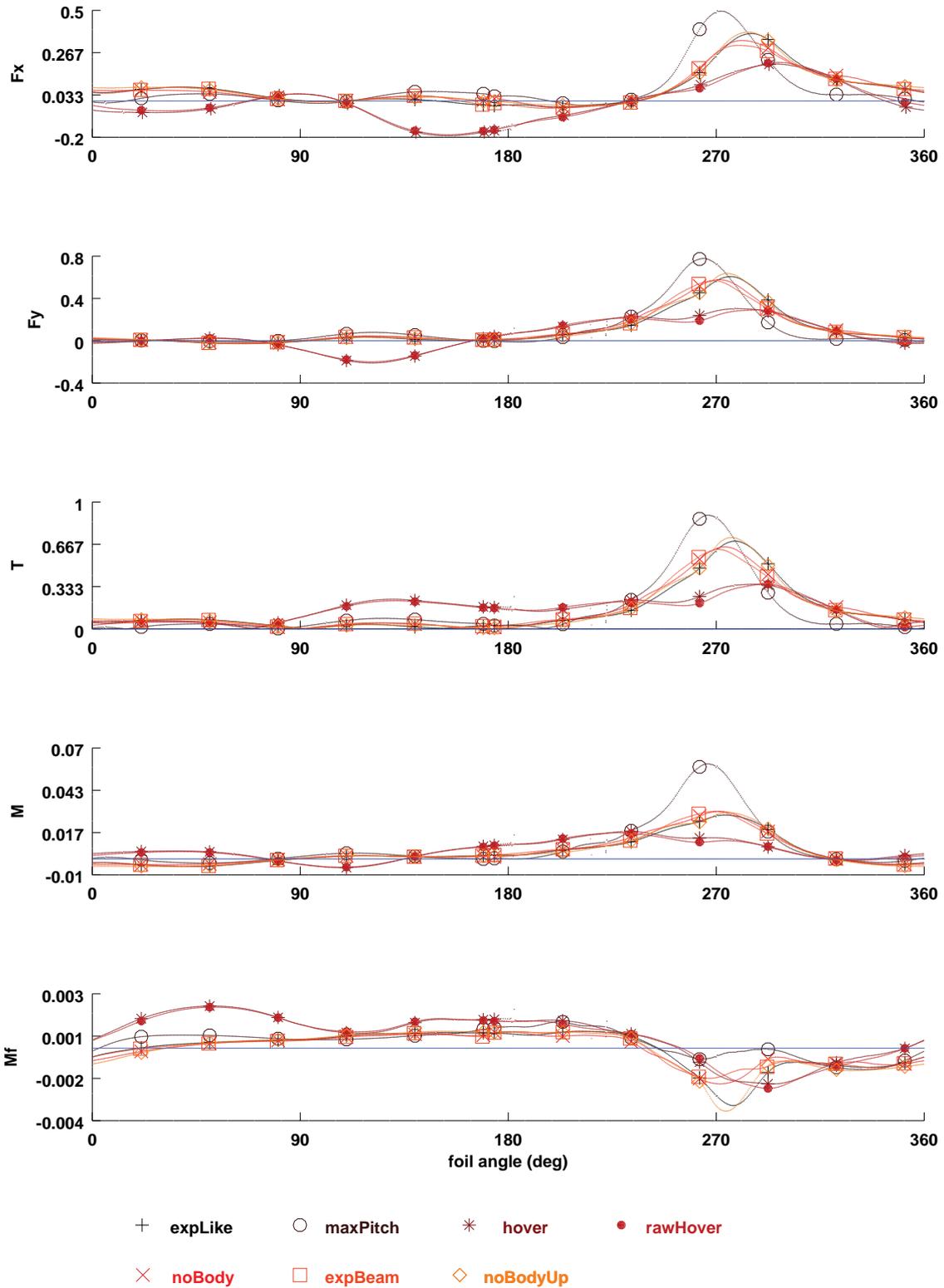
Figure 23: Forces on blade 1 of the front rotor: [Fx - the longitudinal forces], [Fy - the vertical forces], [T - the thrust in the x-y plane], [M - the moment in z about the center of the rotor], [Mf - the moment in z about the pivot center of the blade], plotted against the angle between the rear rotor's blade 1 arm and the positive x-axis. Period going from 6.234 to 7.227 rotation cycles.
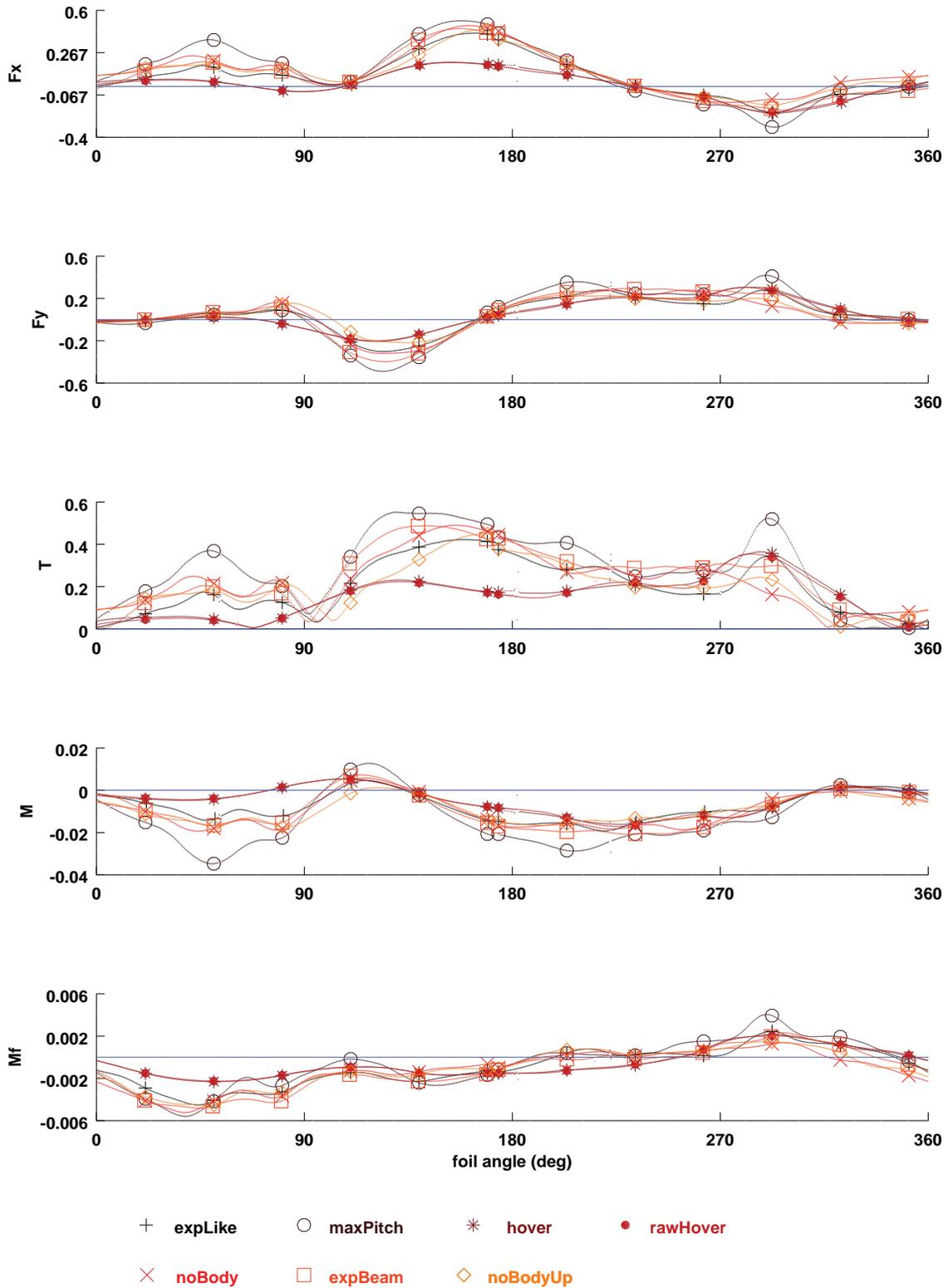
Figure 24: Forces on blade 1 of the rear rotor: [Fx - the longitudinal forces], [Fy - the vertical forces], [T - the thrust in the x-y plane], [M - the moment in z about the center of the rotor], [Mf - the moment in z about the pivot center of the blade], plotted against the angle between the rear rotor's blade 1 arm and the positive x-axis. Period going from 6.234 to 7.227 rotation cycles.
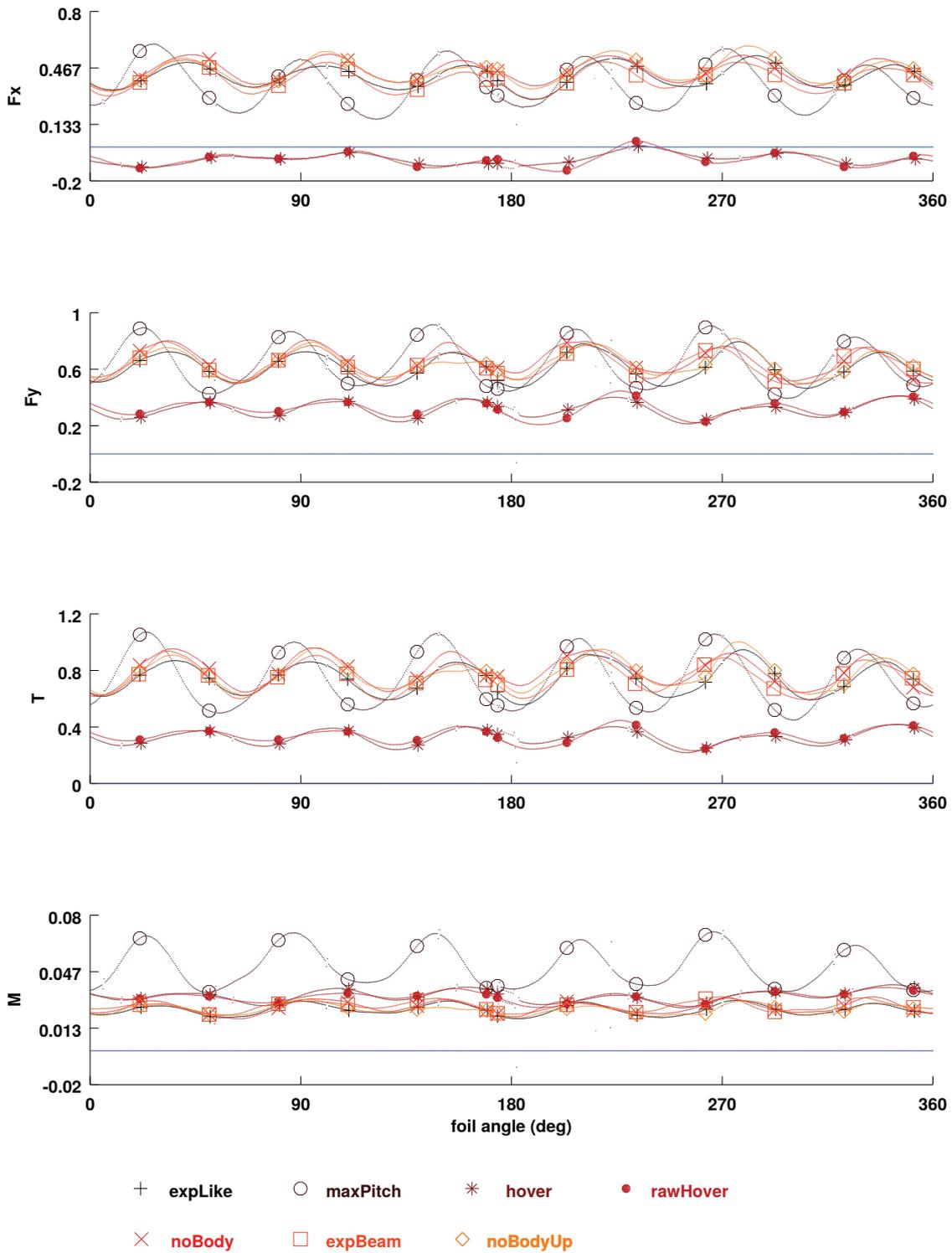
Figure 25: Forces on the front rotor including its endplates: [Fx - the longitudinal forces], [Fy - the vertical forces], [T - the thrust in the x-y plane], [M - the moment in z about the center of the rotor], plotted against the angle between the rear rotor's blade 1 arm and the positive x-axis. Period going from 6.234 to 7.227 rotation cycles.
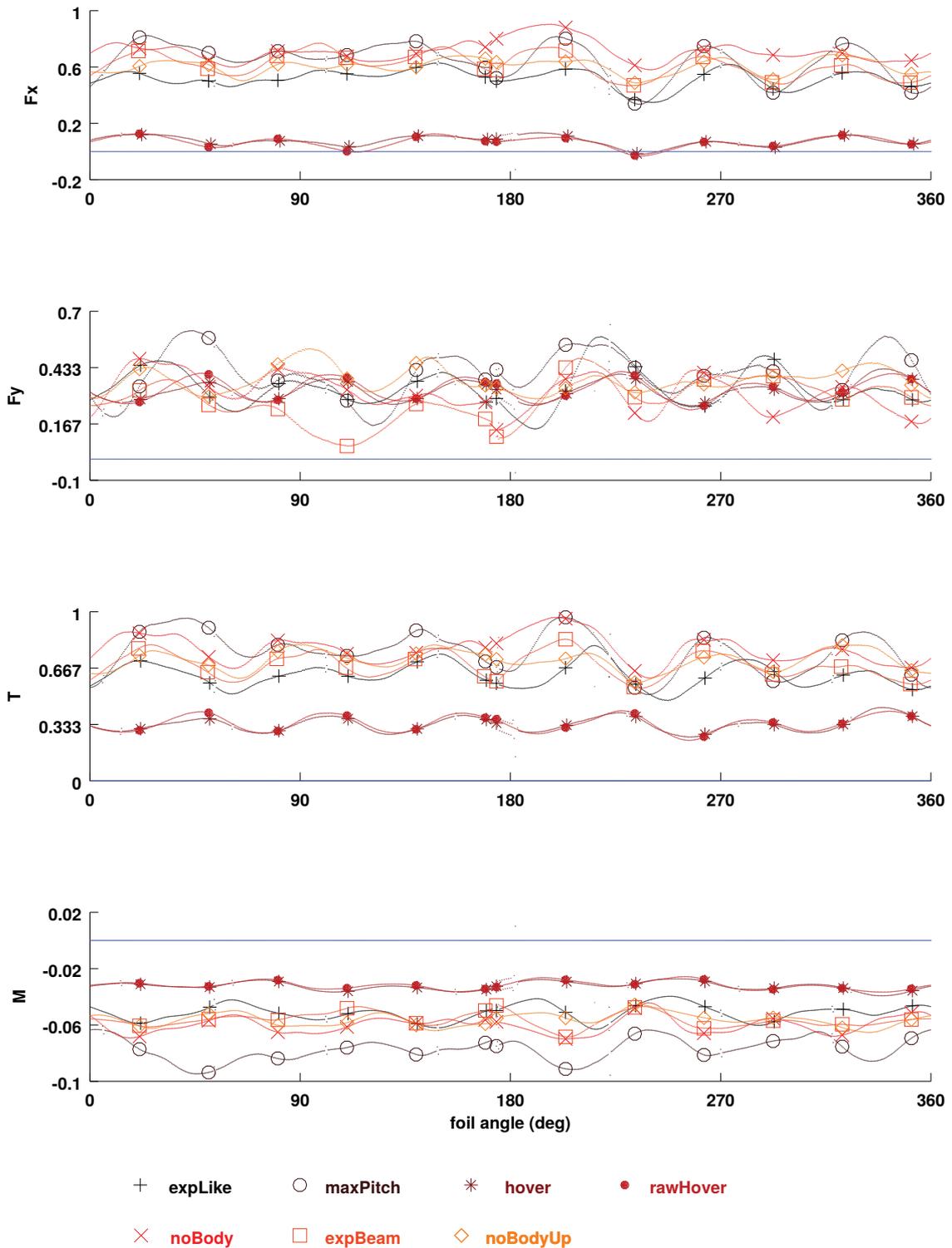
Figure 26: Forces on the rear rotor including its endplates: [Fx - the longitudinal forces], [Fy - the vertical forces], [T - the thrust in the x-y plane], [M - the moment in z about the center of the rotor], plotted against the angle between the rear rotor's blade 1 arm and the positive x-axis. Period going from 6.234 to 7.227 rotation cycles.
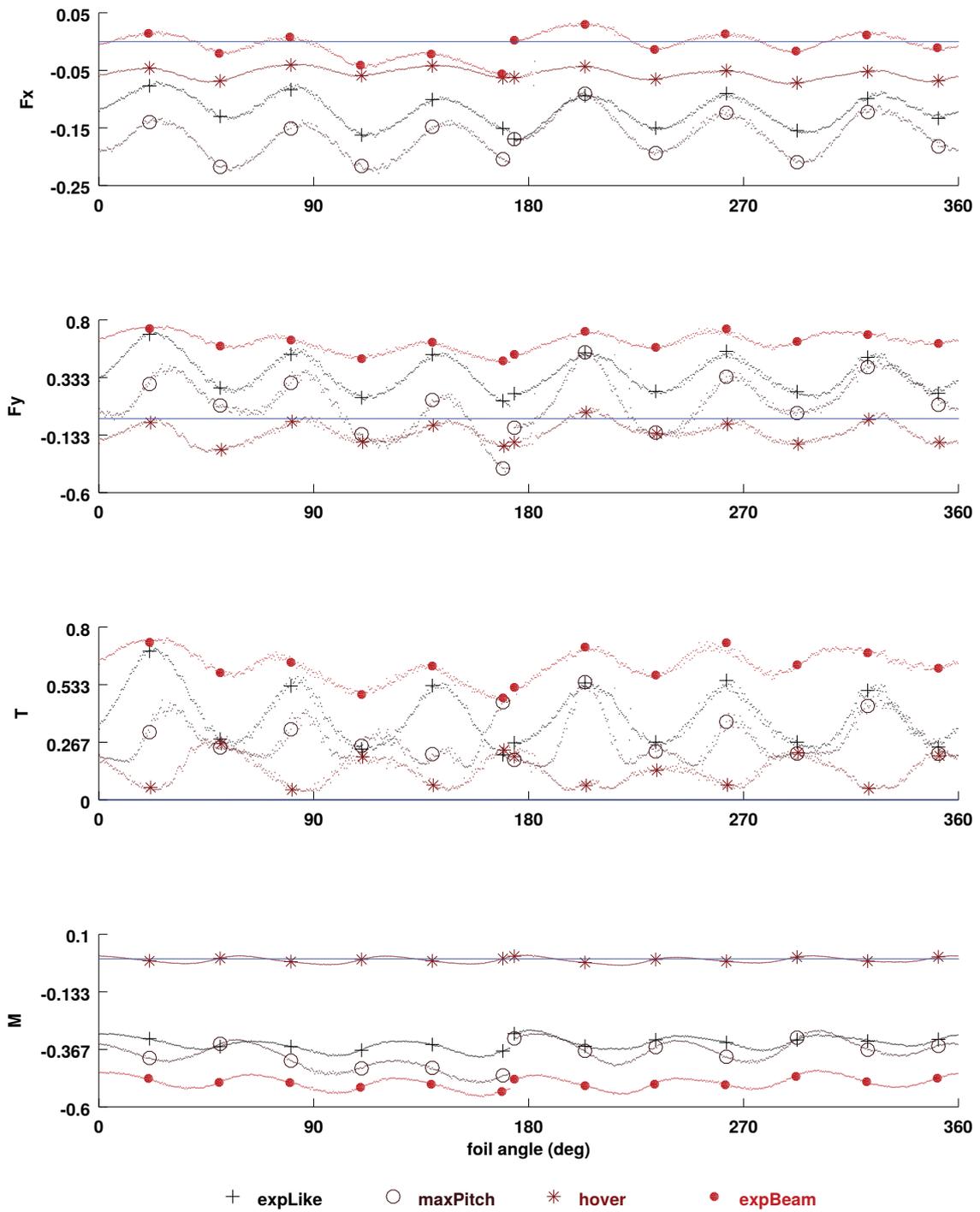
Figure 27: Forces on the half airframe alone multiplied by 2: [Fx - the longitudinal forces], [Fy - the vertical forces], [T - the thrust in the x-y plane], [M - the moment in z about the center point between the rotors], plotted against the angle between the rear rotor's blade 1 arm and the positive x-axis. Period going from 6.234 to 7.227 rotation cycles.

APPENDIX B

Animations are given as supplementary material to complement the analysis provided in this article. They give a visual insight of the interaction between the incoming flow, the front and rear rotors, and the airframe. They use the plane terminology given in Table 7. It is recalled that the videos start when on each rotor blade 1 is positioned as shown in Fig. 9, which corresponds to roughly $173°$ from the positive x-axis for the rear rotor. The videos show one rotor period going from 6.234 to 7.227 rotation cycles, exactly matching the plots shown in APPENDIX A. They are available online at the following URL: http://louisgagnon.com/research/quadcfd/

VID1: Pressure fields at the 3rd x-y plane for the *maxPitch*, *expLike*, *hover*, *noBody*, *noBodyUp*, and *expBeam* cases.

VID2: Velocity fields at the 3rd x-y plane for *maxPitch*, *expLike*, *hover*, *noBody*, *expBeam*, and *rawHover* cases.

VID3: *rawHover* vorticity fields seen in the second y-z plane, the zeroth x-z plane, and the third x-y plane.

VID4: Vorticity fields of the *expLike* case at different x-y planes.

VID5: Vorticity fields of the *hover* case at different x-y planes.

VID6: Vorticity fields of the *expLike* case at different heights of x-z planes.